

# FOURIER BASED FAST MULTIPOLE METHOD FOR THE HELMHOLTZ EQUATION

CRIS CECKA\* AND ERIC DARVE†

**Abstract.** The fast multipole method (FMM) has had great success in reducing the computational complexity of solving the boundary integral form of the Helmholtz equation. We present a formulation of the Helmholtz FMM that uses Fourier basis functions rather than spherical harmonics. By modifying the transfer function in the precomputation stage of the FMM, time-critical stages of the algorithm are accelerated by causing the interpolation operators to become straightforward applications of fast Fourier transforms, retaining the diagonality of the transfer function, and providing a simplified error analysis. Using Fourier analysis, constructive algorithms are derived a priori to determine an integration quadrature for a given error tolerance. Sharp error bounds are derived and verified numerically. Various optimizations are considered to reduce the number of quadrature points and reduce the cost of computing the transfer function.

**Key words.** fast multipole method, fast Fourier transform, Fourier basis, interpolation, antepolation, Helmholtz, Maxwell, integral equations, boundary element method

**AMS subject classifications.** 31B10, 42B10, 65D05, 65R20, 65Y20, 65T40, 70F10, 78M15, 78M16

**1. Introduction.** Since the development of the fast multipole method (FMM) for the wave equation in [19, 5, 20, 10, 18], the FMM has proven to be a very effective tool for solving scalar acoustic and vector electromagnetic problems. In this paper, we consider the application of the FMM to the scalar Helmholtz equation, although our results can be immediately extended to the vector case as described in [3, 7]. The application of the boundary element method to solve the integral form of the Helmholtz equation results in a dense linear system which can be solved by iterative methods such as GMRES or BCGSTAB. These methods require computing dense matrix-vector products which, using a direct implementation, are performed in  $\mathcal{O}(N^2)$  floating-point operations. The FMM uses an approximation of the dense matrix to perform the product in  $\mathcal{O}(N \log N)$  operations. This approximation is constructed from close-pair interactions and far-field approximations represented by spherical integrals that are accumulated and distributed through the domain via an octree.

There are a number of difficulties in implementing the FMM, each of which must be carefully considered and optimized to achieve the improved complexity. The most significant complication in the Helmholtz FMM is that the quadrature sampling rate must increase with the size of the box in the octree, requiring interpolation and antepolation algorithms to transform the data between spherical quadratures of different levels of the tree. Local algorithms such as Lagrange interpolation and techniques which sparsify interpolant matrices are fast, but incur significant errors [16, 7]. Spherical harmonic transforms are global interpolation schemes and are exact but require fast versions for efficiency of the FMM. Many of these fast spherical transform algorithms are only approximate, complicated to implement or use, and not always stable [8, 13, 24].

In this paper, we use a multipole expansion which allows the use of 2D fast Fourier transforms (FFT) in the spherical coordinate system  $(\phi, \theta)$ . The main advantages are

---

\*Institute for Computational and Mathematical Engineering, Stanford University ().

†Institute for Computational and Mathematical Engineering, Mechanical Engineering Department, Stanford University (darve@stanford.edu)

Notation	Description
$\kappa$	wavenumber, $2\pi/\lambda$ with wavelength $\lambda$
$a_l$	box size at level $l$ . Root: $l = 0$ . Highest active level: $l = 2$ .
$\theta$	polar angle
$\phi$	azimuthal angle
$\bar{c}$	complex conjugate of $c$
$\mathbf{x}$	vector in $\mathbb{R}^3$ , $\mathbf{x} =  \mathbf{x}  \hat{\mathbf{x}}$
$\mathbf{x} \cdot \mathbf{y}$	inner product, $\mathbf{x} \cdot \mathbf{y} =  \mathbf{x}   \mathbf{y}  \cos(\varphi_{\mathbf{x}, \mathbf{y}})$
$S^2$	sphere, $\{\hat{\mathbf{s}} \in \mathbb{R}^3 :  \hat{\mathbf{s}}  = 1\}$
$j_n$	spherical Bessel function of the first kind
$y_n$	spherical Bessel function of the second kind
$h_n^{(1)}$	spherical Hankel function of the first kind
$P_n$	Legendre polynomial
$\mathcal{F}_n^x[f]$	$n$ th coefficient of $f$ 's Fourier series in $x$ , $f(x) = \sum_n \mathcal{F}_n^x[f] e^{inx}$

TABLE 1.1  
Table of notations

45 two fold: i) high performance FFT libraries are available on practically all computer  
46 platforms, resulting in accurate, robust, and fast interpolation algorithms; ii) the  
47 resulting error analysis is simplified and leads to sharp, a priori error bounds on the  
48 FMM. One of the difficulties in using FFTs is that we are forced to use a uniform  
49 distribution of points along  $\phi$  and  $\theta$  in the spherical quadrature. Naively, this leads  
50 to a much increased quadrature size for a given accuracy compared to the original  
51 spherical harmonics-based FMM. The reason is as follows. The multipole expansion  
52 in the high frequency regime is derived from:

$$\frac{e^{i\kappa|\mathbf{r}+\mathbf{r}_0|}}{|\mathbf{r}+\mathbf{r}_0|} = \int_{\phi=0}^{2\pi} \int_{\theta=0}^{\pi} e^{i\kappa\hat{\mathbf{s}}\cdot\mathbf{r}} T_{\ell, \mathbf{r}_0}(\hat{\mathbf{s}}) \sin(\theta) d\theta d\phi$$

53 where  $\hat{\mathbf{s}} = [\cos(\phi)\sin(\theta), \sin(\phi)\sin(\theta), \cos(\theta)]$  is the spherical unit vector. It is ap-  
54 parent that we are integrating along  $\theta$  a function which has period  $2\pi$ . However the  
55 bounds of the integral are 0 to  $\pi$ , over which interval the function has a discontinuity  
56 in its derivative. This results in a slow decay of the Fourier spectrum (essentially  
57  $1/\text{freq}^2$ ) of the integrand. Consequently, a large number of quadrature points along  $\theta$   
58 are required.

59 We propose to use a variant of the scheme by J. Sarvas in [22] whereby the  
60 integration is extended from 0 to  $2\pi$  and the integrand modified:

$$\frac{e^{i\kappa|\mathbf{r}+\mathbf{r}_0|}}{|\mathbf{r}+\mathbf{r}_0|} = \frac{1}{2} \int_{\phi=0}^{2\pi} \int_{\theta=0}^{2\pi} e^{i\kappa\hat{\mathbf{s}}\cdot\mathbf{r}} T_{\ell, \mathbf{r}_0}(\hat{\mathbf{s}}) |\sin(\theta)| d\theta d\phi \quad (1.1)$$

61 We will describe in more details how an efficient scheme can be derived from this  
62 equation. The key property is that  $e^{i\kappa\hat{\mathbf{s}}\cdot\mathbf{r}}$  is approximately bandlimited in  $\theta$  and  
63 therefore it is possible to remove the high frequency components of  $T_{\ell, \mathbf{r}_0}(\hat{\mathbf{s}})|\sin(\theta)|$   
64 without affecting the accuracy of the approximation. Using this smooth transfer  
65 function, which is now bandlimited in Fourier space, the number of quadrature points  
66 can be reduced dramatically. We show that the resulting number of quadrature points  
67 is reduced by about 40% compared to the original spherical harmonics-based FMM.

68 Consequently, we now have a scheme which requires few quadrature points and enables  
69 the use of efficient FFT routines.

70 The approach in [22] is similar. However, rather than smoothing  $T_{\ell, r_0}(\hat{s}) |\sin(\theta)|$   
71 once during the precomputation phase as we detail in this paper, Sarvas instead  
72 incorporates the  $|\sin(\theta)|$  factor during the run-time phase of the FMM after the appli-  
73 cation of the transfer function. Although a detailed analysis is required for accurately  
74 assessing the relative cost of the two approaches, the technique in [22] requires ap-  
75 proximately 1.5 times more sample points in the time-critical transfer pass of the  
76 algorithm, and requires an extra antepole step after applying  $T$  with about twice  
77 more sample points than used for the method in this paper. We also note that the  
78 error analysis for the two methods is different, and is easier to carry out with the  
79 approach in this paper.

80 We derive a new a priori error analysis which incorporates both effects from  
81 truncation of the Gegenbauer series (a problem well analyzed [3]) and the numerical  
82 quadrature. Our algorithm to predict the error is very sharp. The sharp bounds  
83 allow the method to choose a minimal number of quadrature points to guarantee a  
84 prescribed error. By comparison, the conventional approach leads to less accurate  
85 estimates resulting in either lower accuracy than requested or higher computational  
86 cost (over-estimation of the required approximation order). Although not consid-  
87 ered in this paper, our error analysis approach can also be applied to the spherical  
88 harmonics-based FMM to yield similarly accurate error bounds. This has practical  
89 importance since it allows guaranteeing the error in the calculation while reducing  
90 the computational cost.

91 The novel contributions of this paper can be summarized as follows:

- 92 • Development of an efficient Helmholtz multi-level FMM which uses FFTs in  
93 the inter/antepole steps while retaining diagonal transfer and translation  
94 functions. The use of FFTs allows leveraging high performance FFT libraries  
95 available for most machines, sequential and parallel.
- 96 • An error analysis that accounts for all error in the method and yields con-  
97 structive algorithms to choose optimal method parameters.
- 98 • Details of various optimizations to reduce the computational cost (e.g. use of  
99 symmetries in the precomputation of the transfer functions, use of symme-  
100 tries on the unit sphere for the inter/antepole steps, optimization of the  
101 quadrature points near the poles of the unit sphere).
- 102 • Pseudocodes are provided to clarify the method and help with an implemen-  
103 tation by the reader.
- 104 • Demonstration of the sharpness of the error bound and the asymptotic com-  
105 putational cost.

106 The paper is organized as follows. In Section 2, we introduce the critical parts  
107 of the classical Helmholtz FMM including the Gegenbauer series truncation (2.1),  
108 the spherical quadrature (2.2), and a short overview of interpolation/antepole  
109 strategies (2.3). Section 3 details the Fourier basis approach. The transfer function  
110 must be modified to lower the computational cost and obtain a competitive scheme,  
111 as detailed in Section 3.2. Section 3.3 analyzes the integration error to derive an  
112 algorithm which determines a quadrature with a prescribed error tolerance. The FFT  
113 based interpolation and antepole algorithms are described in Section 3.4 and  
114 numerical results are given in Section 3.5. Table 1.1 lists the notations used in this  
115 paper.

116 **2. The Multilevel Fast Multipole Method.** The FMM reduces the compu-  
117 tational complexity of the matrix-vector multiplication

$$\sigma_i = \sum_{j \neq i} \frac{e^{i\kappa|\mathbf{x}_i - \mathbf{x}_j|}}{|\mathbf{x}_i - \mathbf{x}_j|} \psi_j \quad (2.1)$$

118 for  $i, j = 1, \dots, N$  from  $\mathcal{O}(N^2)$  to  $\mathcal{O}(N \log N)$ . This improvement is based on the  
119 Gegenbauer series

$$\frac{e^{i\kappa|\mathbf{r} + \mathbf{r}_0|}}{|\mathbf{r} + \mathbf{r}_0|} = i\kappa \sum_{n=0}^{\infty} (-1)^n (2n+1) h_n^{(1)}(\kappa|\mathbf{r}_0|) j_n(\kappa|\mathbf{r}|) P_n(\hat{\mathbf{r}} \cdot \hat{\mathbf{r}}_0) \quad (2.2)$$

120 The series converges absolutely and uniformly for  $|\mathbf{r}_0| \geq \frac{2}{\sqrt{3}}|\mathbf{r}|$  and has been studied  
121 extensively in [2, 6].

122 Truncating the Gegenbauer series at  $\ell$  and using an integral over the unit sphere,  
123  $S^2$ :

$$\frac{e^{i\kappa|\mathbf{r} + \mathbf{r}_0|}}{|\mathbf{r} + \mathbf{r}_0|} = \int_{S^2} e^{i\kappa\hat{\mathbf{s}} \cdot \mathbf{r}} T_{\ell, \mathbf{r}_0}(\hat{\mathbf{s}}) dS(\hat{\mathbf{s}}) + \varepsilon_G$$

124 where  $\varepsilon_G$  is the Gegenbauer series truncation error and the transfer function,  $T_{\ell, \mathbf{r}_0}(\hat{\mathbf{s}})$ ,  
125 is defined as

$$T_{\ell, \mathbf{r}_0}(\hat{\mathbf{s}}) = \frac{i\kappa}{4\pi} \sum_{n=0}^{\ell} i^n (2n+1) h_n^{(1)}(\kappa|\mathbf{r}_0|) P_n(\hat{\mathbf{s}} \cdot \hat{\mathbf{r}}_0). \quad (2.3)$$

126 The reduced computational complexity of the FMM is achieved by constructing a  
127 tree of nodes, typically an octree, over the domain of the source and field points. We  
128 recall the main steps of the FMM to set some notations. Let  $M_{\alpha}^l(\hat{\mathbf{s}})$  be the outgoing  
129 field for  $B_{\alpha}^l$ , the box  $\alpha$  of the tree in level  $l \in [0, L]$  with center  $\mathbf{c}_{\alpha}^l$ .

130 **Initialization:** The method is initialized by computing the outgoing plane-wave  
131 expansions for each cluster contained in a leaf of the tree:

$$M_{\alpha}^L(\hat{\mathbf{s}}) = \sum_{i, \mathbf{x}_i \in B_{\alpha}^L} \psi_i e^{i\kappa\hat{\mathbf{s}} \cdot (\mathbf{x}_i - \mathbf{c}_{\alpha}^L)}$$

132 **Upward Pass (M2M):** These outgoing expansions are then aggregated upward  
133 through the tree by accumulating the product of the child cluster expansions with the  
134 plane-wave translation function:

$$M_{\alpha}^{l-1}(\hat{\mathbf{s}}) = \sum_{\beta, B_{\beta}^l \subset B_{\alpha}^{l-1}} M_{\beta}^l(\hat{\mathbf{s}}) e^{i\kappa\hat{\mathbf{s}} \cdot (\mathbf{c}_{\beta}^l - \mathbf{c}_{\alpha}^{l-1})} \quad l = L, L-1, \dots, 3$$

135 **Transfer Pass (M2L):** Incoming expansions,  $I_{\alpha}^l(\hat{\mathbf{s}})$  of box  $B_{\alpha}^l$ , are computed from  
136 the outgoing by multiplication with the transfer function:

$$I_{\alpha}^l(\hat{\mathbf{s}}) = \sum_{\beta \in \mathcal{I}(B_{\alpha}^l)} M_{\beta}^l(\hat{\mathbf{s}}) T_{\ell, \mathbf{c}_{\beta}^l - \mathbf{c}_{\alpha}^l}(\hat{\mathbf{s}}) \quad l = L, L-1, \dots, 2$$

137 where  $\mathcal{I}(B_{\alpha}^l)$  is the interaction list of box  $B_{\alpha}^l$ , defined as all boxes of level  $l$  which are  
138 not neighbors of  $B_{\alpha}^l$ , but whose parent is a neighbor of the parent of  $B_{\alpha}^l$ .

139 **Downward Pass (L2L):** The incoming expansions are then disaggregated downward  
 140 through the tree to compute the local field  $L_\alpha^l(\hat{\mathbf{s}})$  of box  $B_\alpha^l$ :

$$L_\alpha^{l+1}(\hat{\mathbf{s}}) = L_\beta^l(\hat{\mathbf{s}}) e^{i\kappa\hat{\mathbf{s}} \cdot (\mathbf{c}_\beta^l - \mathbf{c}_\alpha^{l+1})} + I_\alpha^{l+1}(\hat{\mathbf{s}}) \quad l = 2, 3, \dots, L-1$$

141 where  $B_\alpha^{l+1} \subset B_\beta^l$ .

142 **Field Computation:** At the finest level, the integration over the sphere is finally  
 143 performed and added to the near-field contribution to determine the field value at the  
 144  $N$  field points:

$$\sigma_i = \int_{S^2} L_\alpha^L(\hat{\mathbf{s}}) e^{i\kappa\hat{\mathbf{s}} \cdot (\mathbf{c}_\alpha^L - \mathbf{x}_i)} dS(\hat{\mathbf{s}}) + \sum_{\substack{j, j \neq i, \\ \mathbf{x}_j \in \mathcal{N}(B_\alpha^L)}} \frac{e^{i\kappa|\mathbf{x}_i - \mathbf{x}_j|}}{|\mathbf{x}_i - \mathbf{x}_j|} \psi_j \quad (2.4)$$

145 where  $\mathbf{x}_i \in B_\alpha^L$  and  $\mathcal{N}(B_\alpha^L)$  is the neighbor list of  $B_\alpha^L$ , defined as  $B_\alpha^L$  and all neighbor  
 146 boxes of  $B_\alpha^L$ .

147 **2.1. Truncation Parameter in the FMM.** The truncation parameter  $\ell$  must  
 148 be chosen so that the Gegenbauer series (2.2) is converged to a desired accuracy.  
 149 However, for  $n > x$ ,  $j_n(x)$  decreases super-exponentially while  $h_n^{(1)}(x)$  diverges. The  
 150 divergence of the Hankel function causes the transfer function to oscillate wildly and  
 151 become numerically unstable. Even though the expansion converges, roundoff errors  
 152 will adversely affect the accuracy if  $\ell$  is too large. Thus, while one must choose  
 153  $\ell > \kappa|\mathbf{r}|$  so that sufficient convergence of the Gegenbauer series is achieved, it must  
 154 also be small enough to avoid the divergence of the transfer function. The selection of  
 155 the truncation parameter  $\ell$  has been studied extensively and a number of procedures  
 156 for selecting it have been proposed [5, 6].

157 The excess bandwidth formula (EBF) is derived from the convergence of the  
 158 plane-wave spectrum as presented in [3]. The EBF chooses  $\ell$  as

$$\ell \approx \kappa|\mathbf{r}| + C(\kappa|\mathbf{r}|)^{1/3} \quad (2.5)$$

159 An empirically determined common choice is  $C = 1.8(d_0)^{2/3}$ , where  $d_0$  is the desired  
 160 number of digits of accuracy. The EBF is one of the most popular choices to select  
 161 the truncation parameter [12].

162 The actual Gegenbauer truncation error for a given  $\ell$  can also be approximated.  
 163 As Carayol and Collino showed in [2], an upper bound of this error for large values of  
 164  $|\mathbf{r}|$  is obtained when  $P_n(\hat{\mathbf{r}} \cdot \hat{\mathbf{r}}_0) = (\pm 1)^n$  so that

$$|\varepsilon_G| \lesssim \kappa \left| \sum_{n=\ell+1}^{\infty} (\mp 1)^n (2n+1) h_n^{(1)}(\kappa|\mathbf{r}_0|) j_n(\kappa|\mathbf{r}|) \right|$$

165 which they showed can be computed in closed form

$$= \kappa^2 \frac{|\mathbf{r}||\mathbf{r}_0|}{|\mathbf{r}_0| \pm |\mathbf{r}|} \left| h_{\ell+1}^{(1)}(\kappa|\mathbf{r}_0|) j_\ell(\kappa|\mathbf{r}|) \pm h_\ell^{(1)}(\kappa|\mathbf{r}_0|) j_{\ell+1}(\kappa|\mathbf{r}|) \right| \quad (2.6)$$

166 This fails for small  $|\mathbf{r}|$  when the upper bound is obtained by choosing  $\hat{\mathbf{r}} \cdot \hat{\mathbf{r}}_0$  such that  
 167 the oscillation of  $P_n(\hat{\mathbf{r}} \cdot \hat{\mathbf{r}}_0)$  compensates for the oscillation of  $(-1)^n h_n^{(1)}(\kappa|\mathbf{r}_0|) j_n(\kappa|\mathbf{r}|)$ .  
 168 Using the EBF as an initial guess for  $\ell$  and refining the choice using the above closed

169 form when  $|\mathbf{r}|$  is sufficiently large is a simple algorithm which yields a nearly optimal  
 170 value for  $\ell$  (that is the smallest value consistent with the target error). This is the  
 171 scheme we selected for this paper.

172 Carayol and Collino in [1] and [2] present an in-depth analysis of the Jacobi-Anger  
 173 series and the Gegenbauer series. They find the asymptotic formula

$$\ell \approx \kappa |\mathbf{r}| - \frac{1}{2} + \left(\frac{1}{2}\right)^{5/3} W^{2/3} \left( \frac{\kappa |\mathbf{r}|}{4\varepsilon^6} \left( \frac{1 + |\mathbf{r}_0|/|\mathbf{r}|}{1 - |\mathbf{r}_0|/|\mathbf{r}|} \right)^{3/2} \right)$$

174 where  $W(x)$  is the Lambert function defined as the solution to

$$W(x)e^{W(x)} = x \quad x > 0$$

175 This appears to be near optimal for large box sizes.

176 The errors introduced by this truncation have been investigated in other papers  
 177 including [16, 2, 6].

178 **2.2. Spherical Quadrature in the FMM.** The error analysis is simplified if a  
 179 scheme is used which exactly integrates spherical harmonics,  $Y_n^m$ , up to some degree.  
 180 The most common choice of quadrature uses uniform sample points in  $\phi$  and Gauss-  
 181 Legendre sample points in  $z(\theta)$ . With  $N + 1$  uniform points in the  $\phi$  direction and  
 182  $\frac{N+1}{2}$  Gauss-Legendre points in the  $\theta$  direction, all  $Y_n^m$ ,  $-n \leq m \leq n$ ,  $0 \leq n \leq N$  are  
 183 integrated exactly [7, 16].

184 **2.3. Interpolation and Anterpolation in the FMM.** The quadrature sam-  
 185 pling rate depends on the spectral content of the translation operator,  $e^{i\kappa \hat{\mathbf{s}} \cdot \mathbf{r}}$ . Its  
 186 coefficient in the spherical harmonic expansion decreases super-exponentially roughly  
 187 for  $n \gtrsim \kappa |\mathbf{r}|$ . Therefore, as fields are aggregated in the upward pass and  $|\mathbf{r}|$  becomes  
 188 larger, a larger quadrature is required to resolve higher modes. These modes must  
 189 be resolved since they interact with the modes in the transfer function, which do not  
 190 significantly decay as  $\ell$  increases.

191 Similarly, as fields are disaggregated in the downward pass,  $|\mathbf{r}|$  becomes smaller  
 192 and the higher modes of the incoming field make vanishingly small contributions to  
 193 the integral as a consequence of Parseval's theorem. Thus, as the incoming field  
 194 is disaggregated down the tree, a smaller quadrature can be used to resolve it. This  
 195 makes the integration faster and is actually required to achieve an optimal asymptotic  
 196 running time. See Table 2.1.

197 There have been several approaches to performing the interpolation and anter-  
 198 polation between levels in the FMM. Below, we enumerate a number of options that  
 199 have previously been studied.

200 General, local interpolation methods like Lagrange interpolation, Gaussian inter-  
 201 polation, and B-splines are fast and provide for simple error analysis [16].

202 A spherical harmonic transform maps function values  $f_k$ , sampled at  $(\phi_k, \theta_k)$ , to  
 203 a new quadrature  $(\phi'_{k'}, \theta'_{k'})$ , via the linear transformation

$$f_{k'} = \sum_{m,l \leq K} Y_l^m(\phi'_{k'}, \theta'_{k'}) \sum_k \omega_k \overline{Y_l^m(\phi_k, \theta_k)} f_k = \sum_k A_{k'k} f_k \quad (2.7)$$

204 This results in an  $\mathcal{O}(N \log N)$  or  $\mathcal{O}(N^{3/2})$  FMM (see Table 2.1). Fast spherical  
 205 transforms (FST) have been developed in [8, 13, 24, 21] and applied to the FMM in [4].  
 206 Using the FST reduces the interpolation and anterpolation procedures to  $\mathcal{O}(K \log K)$ ,

207 which results in an  $\mathcal{O}(N \log^2 N)$  FMM. However, the accuracy and stability of these  
 208 algorithms remain in question.

209 Approximations of the spherical transform have also been investigated in [14, 7].  
 210 The interpolation matrix  $A_{k'k}$  in (2.7) can be sparsified in a number of ways to provide  
 211 an interpolation/antepolation method that scales as  $\mathcal{O}(K)$  with controllable relative  
 212 error. Many other interpolation schemes exist with varying running times and errors.  
 213 Rokhlin presents a fast polynomial interpolator based on the fast multipole method  
 214 in [9]. See also [15].

215 The asymptotic computational complexity in the big-O sense is summarized in  
 216 Table 2.1.

Interpolation	Volume	Surface
Direct	$N \log N$	$N^{3/2}$
Fast Global	$N$	$N \log^2 N$
Local	$N$	$N \log N$

TABLE 2.1

*Computational complexity in the big-O sense. Column 2 and 3 refer to the distribution of particles. We assume that  $N = \mathcal{O}((\kappa a_0)^3)$  for a volume of scatterers and  $N = \mathcal{O}((\kappa a_0)^2)$  for a surface of scatterers. Direct refers to a computation of the operator with no acceleration (basically several matrix vector products). Fast Global refers to fast spherical harmonic transforms or fast Fourier transforms (this work). Local are methods based on local interpolation such as using Lagrange interpolation.*

217 **3. Fourier Based Multilevel Fast Multipole Method.** The Fourier based  
 218 fast multipole method is based on the identity

$$\int_{S^2} e^{i\kappa \hat{\mathbf{s}} \cdot \mathbf{r}} T_{\ell, \mathbf{r}_0}(\hat{\mathbf{s}}) dS(\hat{\mathbf{s}}) = \int_0^{2\pi} \int_0^{2\pi} E_{\mathbf{r}}(\theta, \phi) T_{\ell, \mathbf{r}_0}^{\mathbf{s}}(\theta, \phi) d\phi d\theta \quad (3.1)$$

219 where the translation function  $E_{\mathbf{r}}(\theta, \phi)$  and the modified transfer function  $T_{\ell, \mathbf{r}_0}^{\mathbf{s}}(\theta, \phi)$   
 220 are defined as

$$E_{\mathbf{r}}(\theta, \phi) = e^{i\kappa \hat{\mathbf{s}} \cdot \mathbf{r}} \quad T_{\ell, \mathbf{r}_0}^{\mathbf{s}}(\theta, \phi) = \frac{1}{2} T_{\ell, \mathbf{r}_0}(\hat{\mathbf{s}}) |\sin(\theta)| \quad (3.2)$$

221 with  $\hat{\mathbf{s}} = [\cos(\phi) \sin(\theta), \sin(\phi) \sin(\theta), \cos(\theta)]$  and  $T_{\ell, \mathbf{r}_0}(\hat{\mathbf{s}})$  is the transfer function de-  
 222 fined in Equation (2.3). The  $\int_{S^2}$  representation is common and implied throughout  
 223 the discussion in Section 2. The natural basis for integration on the sphere is the  
 224 spherical harmonics  $Y_n^m$  which form an orthonormal basis of  $L^2(S^2)$  and the FMMs  
 225 of Section 2 attempt to preserve this basis expansion in the upward and downward  
 226 pass. The  $\int_0^{2\pi} \int_0^{2\pi}$  representation suggests the use of the Fourier functions  $\{e^{im\phi} e^{im\theta}\}$   
 227 which form an orthonormal basis of  $L^2([0, 2\pi] \times [0, 2\pi])$ . Doubling the sphere to use  
 228 Fourier methods is presented in a more general manner in [22, 23].

229 Using a Fourier basis rather than a spherical harmonics basis allows i) using  
 230 two dimensional uniform quadratures; ii) fast Fourier transforms in the interpolation  
 231 and antepolation steps; and iii) spectral analysis in the error estimates. Of these  
 232 advantages, the most important is that the FFT interpolations and antepolations are  
 233 fast and exact. Since there is no interpolation error, the only significant contributions  
 234 to the final error are the truncation of the Gegenbauer series and the integration  
 235 error due to the finite quadrature. Thus, the error analysis is simplified and we will  
 236 determine in this paper precise bounds on the final error. In fact, our error analysis

237 is fairly general and can be extended to the classical FMM with schemes that exactly  
 238 integrate spherical harmonics (see direct and fast global methods in Section 2.3). The  
 239 result is a fast, easy to implement, and controllable version of the FMM, which we  
 240 detail in the following sections.

### 241 3.1. Fourier Quadratures.

242 **3.1.1. Spherical Fourier.** A periodic complex function defined over  $[0, 2\pi] \times$   
 243  $[0, 2\pi]$  with spherical symmetry,

$$f(\theta, \phi) = f(2\pi - \theta, \pi + \phi) \quad (3.3)$$

244 has the trigonometric polynomial representation

$$f(\theta, \phi) = \sum_{n=-\infty}^{\infty} \sum_{m=-\infty}^{\infty} \tilde{f}_{n,m} e^{i(n\theta+m\phi)} \quad (3.4)$$

245 where the symmetry condition (3.3) is equivalent to

$$\tilde{f}_{n,m} = (-1)^m \tilde{f}_{-n,m} \quad \forall n, m \quad (3.5)$$

246 If functions  $f$  and  $g$  can be represented exactly by trigonometric polynomials of  
 247 degree  $(\tilde{N}_\theta, \tilde{N}_\phi)$  then their  $L^2$  inner-product can be computed exactly as

$$\begin{aligned} \langle f, g \rangle &= \int_0^{2\pi} \int_0^{2\pi} f(\theta, \phi) \overline{g(\theta, \phi)} d\theta d\phi = 4\pi^2 \sum_{n=-\tilde{N}_\theta}^{\tilde{N}_\theta} \sum_{m=-\tilde{N}_\phi}^{\tilde{N}_\phi} \tilde{f}_{n,m} \overline{\tilde{g}_{n,m}} \\ &= \frac{4\pi^2}{N_\theta N_\phi} \sum_{n=1}^{N_\theta} \sum_{m=1}^{N_\phi} f(\theta_n, \phi_m) \overline{g(\theta_n, \phi_m)} \end{aligned}$$

248 where

$$\begin{aligned} N_\theta &= 2\tilde{N}_\theta + 1 & \theta_n &= \frac{2\pi n}{N_\theta} \\ N_\phi &= 2\tilde{N}_\phi + 1 & \phi_m &= \frac{2\pi m}{N_\phi} \end{aligned}$$

249 If  $N_\phi$  is made even (by padding the Fourier coefficients with an extra zero), then

$$f(\theta_n, \phi_m) = f(\theta_{N_\theta-n}, \phi_{N_\phi/2+m}) \quad (3.6)$$

250 so that only half of the sampled values must be stored.

251 **3.1.2. Integration with Fourier Filtering.** A key concern in using the 2D  
 252 Fourier basis rather than the spherical harmonics in Equation (3.1) is the integration  
 253 weight  $\frac{1}{2} |\sin(\theta)|$ . Although the transfer function,  $T_{\ell, \mathbf{r}_0}$  is bandlimited in  $\theta$  and  $\phi$  the  
 254 modified transfer function,  $T_{\ell, \mathbf{r}_0}^s$  is not bandlimited in  $\theta$  due to the integration weight.  
 255 In this section, we review a common strategy for integrating functions that are not  
 256 bandlimited against functions that are bandlimited or nearly bandlimited.

257 Consider the periodic functions

$$f(\theta) = \sum_{n=-\infty}^{\infty} \tilde{f}_n e^{in\theta} \quad g(\theta) = \sum_{m=-\infty}^{\infty} \tilde{g}_m e^{im\theta}$$



258 Note that their exact integral on  $[0, 2\pi]$  is

$$\langle f, g \rangle = \int_0^{2\pi} f(\theta) \overline{g(\theta)} d\theta = 2\pi \sum_{n=-\infty}^{\infty} \tilde{f}_n \overline{\tilde{g}_n} \quad (3.7)$$

259 Computing this integral numerically with a uniform quadrature of size  $K$  yields

$$\begin{aligned} \langle f, g \rangle_K &= \frac{2\pi}{K} \sum_{k=1}^K f(\theta_k) \overline{g(\theta_k)} = \frac{2\pi}{K} \sum_{n=-\infty}^{\infty} \sum_{m=-\infty}^{\infty} \tilde{f}_n \overline{\tilde{g}_m} \sum_{k=1}^K e^{2\pi i(n-m)k/K} \\ &= 2\pi \sum_{n=-\infty}^{\infty} \sum_{m=-\infty}^{\infty} \tilde{f}_n \overline{\tilde{g}_{n+mK}} \end{aligned}$$

260 So the error is exactly given by

$$|\langle f, g \rangle - \langle f, g \rangle_K| = 2\pi \left| \sum_{n=-\infty}^{\infty} \sum_{m \neq 0} \tilde{f}_n \overline{\tilde{g}_{n+mK}} \right| = 2\pi \left| \sum_{n=-\infty}^{\infty} \sum_{m \neq 0} \tilde{f}_{n+mK} \overline{\tilde{g}_n} \right|$$

261 The error is therefore determined by the asymptotic decay of both  $\tilde{f}_n$  and  $\tilde{g}_n$ . For  
 262 example, if  $|\tilde{f}_n|$  decays as  $1/n^\alpha$ ,  $\alpha > 1$ , then  $\sum_n |\tilde{f}_{nK} \tilde{g}_0| \sim 1/K^\alpha$ , which is the  
 263 typically expected decay of the error on a uniform quadrature as a function of  $K$ .  
 264 The equivalent result holds for  $\tilde{g}_n$ . Thus, if the spectrum of either  $f$  or  $g$  decays  
 265 slowly, a very large quadrature  $K$  is needed.

266 However, if the spectrum of  $f$  decays slowly and the spectrum of  $g$  decays quickly  
 267 a much smaller quadrature can be used by truncating the Fourier coefficients of  $f$ .  
 268 Let us define a bandlimited version of  $f(\theta)$

$$f_N(\theta) = \sum_{n=-N}^N \tilde{f}_n e^{in\theta} \quad (3.8)$$

269 and use a uniform quadrature of  $K$  points to compute the integral. Then

$$\langle f_N, g \rangle_K = 2\pi \sum_{n=-N}^N \sum_{m=-\infty}^{\infty} \tilde{f}_n \overline{\tilde{g}_{n+mK}}$$

270 which yields the error

$$|\langle f, g \rangle - \langle f_N, g \rangle_K| = 2\pi \left| \sum_{|n| > N} \tilde{f}_n \overline{\tilde{g}_n} - \sum_{n=-N}^N \sum_{m \neq 0} \tilde{f}_n \overline{\tilde{g}_{n+mK}} \right| \quad (3.9)$$

271 This error can be made small by requiring only that  $\tilde{g}_n$  decays quickly enough. That is,  
 272  $|\tilde{f}_n|$  can decay slowly provided  $|\tilde{g}_n|$  decays quickly. The first term of (3.9) represents  
 273 the truncation error in using the bandlimited  $f_N$  instead of  $f$ . The second term  
 274 represents the aliasing error resulting from the finite sampling of the function  $g$ . As  
 275 an example, if we assume that  $\tilde{g}_n$  is negligible for  $|n| > N$  then it is sufficient to  
 276 choose  $K = 2N + 1$  so that  $|n + mK| > N$  for all  $-N \leq n \leq N$  and  $m \neq 0$  so that  
 277  $\tilde{g}_{n+mK}$  is always negligible.

278 Detailed numerical results will be presented in Section 3.5. However, to demon-  
 279 strate this idea on a simple example, we build a quadrature to calculate:

$$\int_0^{2\pi} |\sin \theta| \cos(64 \cos(\theta)) \, d\theta$$

280 which is a simple model problem for [see Equation (3.1)]

$$\int_0^{2\pi} T_{\ell, \mathbf{r}_0}(\hat{\mathbf{s}}) |\sin \theta| e^{i\kappa \hat{\mathbf{s}} \cdot \mathbf{r}} \, d\theta$$

281 when  $\mathbf{r} = 64/\kappa \hat{\mathbf{z}}$  ( $z$ -axis). Using a uniform quadrature to compute this integral yields  
 282 slow convergence in  $1/N^2$  because the function  $f(\theta) = |\sin \theta|$  is  $C^0$  (see Figure 3.2).  
 283 Instead, if we smooth  $|\sin \theta|$  and remove the high-frequency components following  
 284 Equation (3.8), we obtain a much faster convergence (see Figure 3.2). The number  
 285 of quadrature points is  $K = 2N + 1$ . The Fourier spectrum of  $g(\theta) = \cos(64 \cos(\theta))$   
 286 decays rapidly once  $|n| \gtrsim 64$  (see Figure 3.1). Convergence should occur once  $N \gtrsim 64$   
 287 and this is indeed what is observed in Figure 3.2. The exact value of the integral  
 288  $\sin(64)/16$  is used as the reference solution to calculate the error.

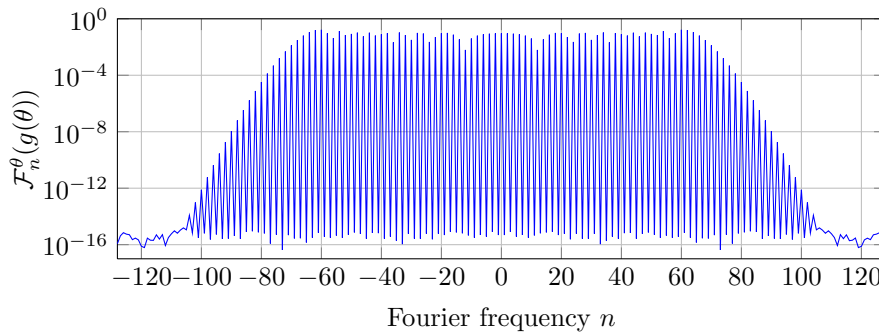


FIG. 3.1. The spectrum of  $g(\theta) = \cos(64 \cos(\theta))$  showing a rapid decay of the coefficients for  $|n| > 64$ . The Fourier spectrum was computed using 256 sample points.

289 The idea of accurately calculating the integral of a product of two functions by  
 290 analytically removing high frequencies in one of the two functions can be found in  
 291 other papers dealing with the fast multipole method for the Helmholtz kernel in the  
 292 high frequency regime, e.g. [7, 6]. In the context of these papers, the smoothing  
 293 operation (removal of high frequencies) is often termed antepolation or subsampling.  
 294 A similar idea is found in Sarvas et al. [22]. In McKay Hyde et al. [17] (Appendix A,  
 295 p. 254–257), this idea is used in the more general context of calculating the integral  
 296 of the product of a discontinuous function with a  $C^1$  piecewise-smooth and periodic  
 297 function.

298 **3.1.3. Fourier Interpolation and Antepolation.** Fast Fourier interpolation  
 299 and antepolation methods are key to creating an efficient Fourier based FMM by  
 300 supersampling trigonometric polynomials and truncating spectral content that does  
 301 not significantly contribute to the final result. A Fourier interpolation pads the Fourier  
 302 coefficients of a function with zeros and increases the sampling rate in real-space.  
 303 A Fourier antepolation removes high frequencies of a function and decreases the  
 304 sampling rate in real-space.

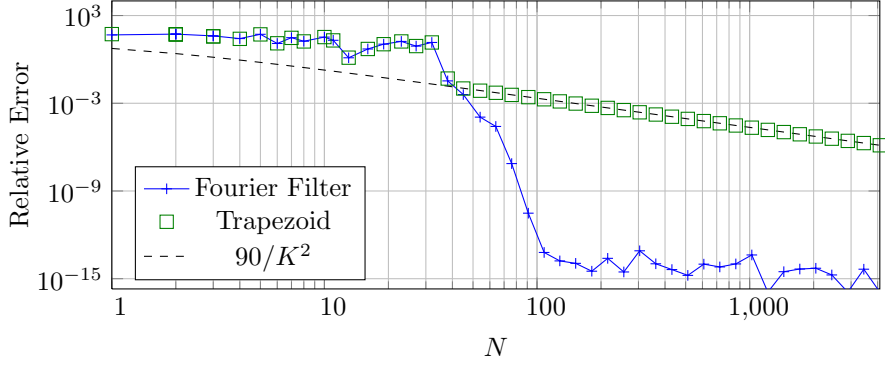


FIG. 3.2. Relative error in the integral as a function of  $N$ . The number of quadrature points is  $K = 2N + 1$ . The blue line integrates the function using a Fourier filter for  $|\sin(\theta)|$  as shown in Equation (3.9). The rapid convergence can be seen after  $N \gtrsim 66$ . The trapezoid method has a slower convergence in  $1/K^2$  because  $|\sin \theta|$  is only  $C^0$ .

305 To motivate the use of Fourier interpolations and antepolations in the Helmholtz  
 306 MLFMM, suppose that the spectrum of  $f_N(\theta)$  is bounded, that is  $|\tilde{f}_n| \leq F$ , and that  
 307  $K = 2N + 1$ , then (3.9) simplifies to

$$|\langle f, g \rangle - \langle f_N, g \rangle_K| \leq 4\pi F \left| \sum_{|n| > N} \tilde{g}_n \right|. \quad (3.10)$$

308 This can be used to find an appropriate truncation parameter  $N$  if  $\tilde{g}_n$  is known or  
 309 can be approximated. The key step to constructing a fast algorithm is to note that  
 310 the Fourier series of  $E_{\mathbf{r}}(\theta, \phi)$  in  $\theta$  decays rapidly while the Fourier series of  $T_{\ell, \mathbf{r}_0}^s(\theta, \phi)$   
 311 in  $\theta$  decays slowly. This is due to the slow decay of the Fourier series of  $|\sin(\theta)|$ :

$$\mathcal{F}_n^\theta[|\sin(\theta)|] = \frac{(-1)^n + 1}{\pi(1 - n^2)} = \begin{cases} \frac{2}{\pi} \frac{1}{1 - n^2} & \text{if } n \text{ even} \\ 0 & \text{if } n \text{ odd} \end{cases}$$

312 The spectrum of the plane-wave is given by

$$E_{\mathbf{r}}(\theta, \phi) = e^{i\kappa|\mathbf{r}|\cos(\varphi_{\hat{\mathbf{s}}, \mathbf{r}})} = \sum_{n=-\infty}^{\infty} i^n J_n(\kappa|\mathbf{r}|) e^{in\varphi_{\hat{\mathbf{s}}, \mathbf{r}}} \quad (3.11)$$

313 where  $\varphi_{\hat{\mathbf{s}}, \mathbf{r}}$  is the angle between  $\hat{\mathbf{s}}$  and  $\mathbf{r}$ . The functions  $J_n$  decay rapidly once  $n > \kappa|\mathbf{r}|$   
 314 resulting in an approximately band-limited function. In the following sections, we use  
 315 the spectral decay of the translation function  $E_{\mathbf{r}}(\theta, \phi)$  (which plays the role of  $g$  in  
 316 the previous section) to determine an appropriate Fourier truncation of the modified  
 317 transfer function,  $T_{\ell, \mathbf{r}_0}^s(\theta, \phi)$  (which plays the role of  $f$ ).

318 Equation (3.10) illustrates the need for interpolation and antepolation as de-  
 319 scribed in Section 2.3 but in the context of the Fourier basis. With  $\tilde{g}_n = \mathcal{F}_n^\theta[E_{|\mathbf{r}|\hat{\mathbf{z}}}] =$   
 320  $i^n J_n(\kappa|\mathbf{r}|)$ , the truncation  $N$  is approximately  $N \gtrsim \kappa|\mathbf{r}| \sim \ell$ . During the upward  
 321 pass,  $|\mathbf{r}|$  increases and we require more modes in  $f = T_{\ell, \mathbf{r}_0}^s$ . During the downward  
 322 pass, the incoming local field,  $L^l$  in Section 2, is to be integrated against translation  
 323 functions of increasingly smaller  $|\mathbf{r}|$ . See Equation (2.4) with  $\mathbf{r} = \mathbf{c}_\alpha^L - \mathbf{x}_i$ . The high  
 324 modes of the field do not significantly contribute to the exact integral (3.7) so the  
 325 field can be safely antepolated at each downward step.

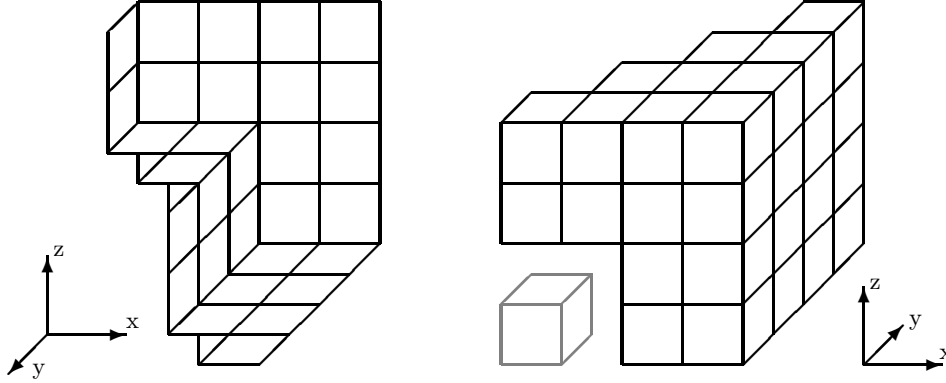


FIG. 3.3. The center of each box represents one transfer vector  $\mathbf{r}_0$  which must be computed. The pictures on the left and right panels represent the same set of boxes viewed under two different angles. Due to the symmetries of the quadrature, we need only compute transfer vectors with  $x, y, z \geq 0$  and  $x \geq y$ . We therefore end up with essentially half of an octant. Specifically, 34 transfer vectors are required; they can be reflected into any of the 316 needed.

326 **3.2. Computing the Bandlimited Modified Transfer Function.** Select a  
 327 2D uniform quadrature with points  $(\theta_n, \phi_m)$  defined by

$$\theta_n = \frac{2\pi n}{N_\theta} \quad \phi_m = \frac{2\pi m}{N_\phi}$$

328 Noting that the plane wave  $E_{\mathbf{r}}(\theta, \phi)$  and modified transfer function  $T_{\ell, \mathbf{r}_0}^s(\theta, \phi)$   
 329 both have spherical symmetry (3.3), the computational and memory cost are reduced  
 330 by requiring  $N_\phi$  to be even so that only half of the quadrature points need to be  
 331 computed and stored.

332 Additionally, in an FMM with a single octree, there are 316 distinct transfer  
 333 vectors  $\mathbf{r}_0$  per level. By enforcing symmetries in the quadrature, the number of  
 334 modified transfer functions that must be precomputed is reduced. Specifically, by  
 335 requiring  $N_\theta$  to be a multiple of 2 and  $N_\phi$  to be a multiple of 4, we enforce reflection  
 336 symmetries in the  $z = 0$ ,  $x = 0$ ,  $y = 0$ ,  $x = y$ , and  $x = -y$  planes. This reduces  
 337 the number of modified transfer functions that need to be precomputed from 316 per  
 338 level to 34 – saving a factor of 9.3 in memory and costing a negligible permutation of  
 339 the values of a computed modified transfer function. See Figure 3.3.

340 Suppose we have chosen a quadrature characterized by  $(N_\theta, N_\phi)$ . Following Sec-  
 341 tion 3.1.2, we need to exactly calculate a bandlimited version of  $T_{\ell, \mathbf{r}_0}^s$ , called  $T_{\ell, \mathbf{r}_0}^{s, L}$ ,  
 342 such that:

$$\mathcal{F}_n^\theta[T_{\ell, \mathbf{r}_0}^{s, L}(\theta, \phi)] = \begin{cases} \mathcal{F}_n^\theta[T_{\ell, \mathbf{r}_0}^s(\theta, \phi)], & |n| \leq N_\theta/2 - 1 \\ 0, & \text{otherwise} \end{cases}$$

343 Since  $T_{\ell, \mathbf{r}_0}$  is bandlimited in  $\theta$  with bandwidth  $2\ell + 1$ , only the frequencies  $|m| \leq$   
 344  $N_\theta/2 + \ell - 1$  of  $|\sin(\theta)|$  contribute to  $T_{\ell, \mathbf{r}_0}^{s, L}$ . Therefore, the exact bandlimited modified  
 345 transfer function,  $T_{\ell, \mathbf{r}_0}^{s, L}$ , can be computed using the pseudocode in Algorithm 1.

- 1  $\tilde{s}_n \leftarrow \mathcal{F}_n^\theta[|\sin(\theta)|] = \frac{(-1)^n+1}{\pi(1-n^2)}$  for all  $|n| \leq N_\theta/2 + \ell - 1$ ;
- 2 **for**  $\phi_m, m = 0, \dots, N_\phi/2 - 1$ , **do**
- 3      $T(\theta_n, \phi_m) \leftarrow \frac{1}{2}T_{\ell, r_0}(\frac{2\pi n}{2\ell+1}, \phi_m), n = 0, \dots, 2\ell$ ;
- 4      $\tilde{T}_n \leftarrow \mathcal{F}_n^\theta[T]$ ;
- 5      $T_n^{s,L} \leftarrow \tilde{s} \otimes \tilde{T}$  convolution of Fourier series;
- 6      $T_n^{s,L} \leftarrow$  truncate to frequencies  $|n| \leq N_\theta/2 - 1$ ;
- 7      $T^{s,L}(\theta_n, \phi_m) \leftarrow$  inverse transform of  $T_n^{s,L}$ ;

**Algorithm 1:** Pseudocode to compute the bandlimited modified transfer function,  $T^{s,L}$ , given  $\ell, r_0, N_\theta$ , and  $N_\phi$ .

Algorithm 1 yields the bandlimited modified transfer function at  $(\theta_n, \phi_m)$ ,  $0 \leq n < N_\theta, 0 \leq m < N_\phi/2$  which can be unwrapped to the remaining points by using the spherical symmetry (3.6). Note that this calculation can also be performed in real-space. It is equivalent to making a Fourier interpolation of  $T_k$  from  $2\ell + 1$  points to  $N_\theta + 2\ell - 1$  points, multiplying by a bandlimited  $|\sin(\theta)|$ , and performing a Fourier anterpolation back to  $N_\theta$  points, as shown in Figure 3.4.

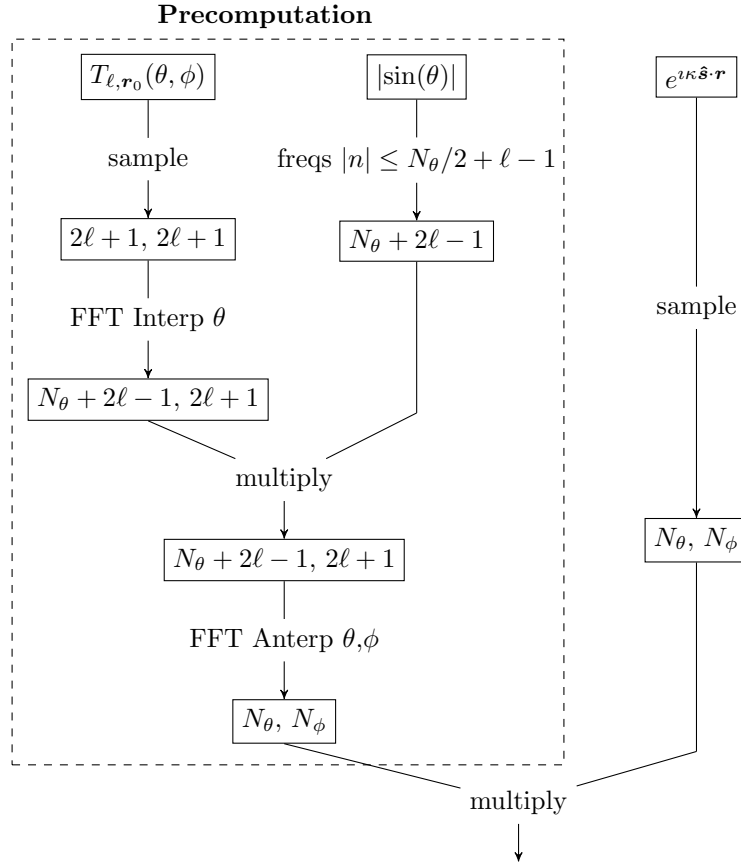


FIG. 3.4. Procedure for precomputing the bandlimited modified transfer function and its application to an outgoing field. The boxed numbers give the numbers of quadrature points for  $\theta$  and  $\phi$  ( $N_\theta$  and  $N_\phi$ ) at each stage.

354 Because sampling the transfer function at a single point is an  $\mathcal{O}(\ell)$  operation  
 355 and  $N_\phi, N_\theta \in \mathcal{O}(\ell)$ , the algorithm as presented is  $\mathcal{O}(\ell^3)$ . The computation of the  
 356 transfer function at all sample points can be accelerated to  $\mathcal{O}(\ell^2)$  as in [11] by taking  
 357 advantage of its symmetry about the  $\hat{\mathbf{r}}_0$  axis and using interpolation algorithms, but  
 358 at the cost of introducing additional error.

359 **3.3. Choice of Quadrature.** The quadrature parameters can be constructively  
 360 computed by determining the maximum error they incur. The error in computing the  
 361 desired integral using the bandlimited modified transfer function with a finite uniform  
 362 quadrature is

$$|\varepsilon_I| = \left| \int_0^{2\pi} \int_0^{2\pi} E_{\mathbf{r}}(\theta, \phi) T_{\ell, \mathbf{r}_0}^s(\theta, \phi) d\phi d\theta - \frac{4\pi^2}{N_\theta N_\phi} \sum_{n=1}^{N_\theta} \sum_{m=1}^{N_\phi} E_{\mathbf{r}}(\theta_n, \phi_m) T_{\ell, \mathbf{r}_0}^{s,L}(\theta_n, \phi_m) \right| \quad (3.12)$$

363 where  $T_{\ell, \mathbf{r}_0}^{s,L}(\theta_n, \phi_m)$  is the bandlimited modified transfer function described in Sec-  
 364 tion 3.2.

365 **3.3.1. Choosing  $N_\theta$ .** The worst-case for  $\varepsilon_I$  in terms of  $N_\theta$  occurs when  $\mathbf{r}$  and  
 366  $\mathbf{r}_0$  are aligned with the  $z$ -axis. This causes all spectral information to be contained in  
 367 the  $\theta$ -direction and makes  $\varepsilon_I$  a function of  $N_\theta$  only. Integrating  $\phi$  out of (3.12) yields

$$|\varepsilon_I^\theta| = 2\pi \left| \int_0^{2\pi} E_{\pm|\mathbf{r}|\hat{\mathbf{z}}}(\theta, 0) T_{\ell, |\mathbf{r}_0|\hat{\mathbf{z}}}^s(\theta, 0) d\theta - \frac{2\pi}{N_\theta} \sum_{n=1}^{N_\theta} E_{\pm|\mathbf{r}|\hat{\mathbf{z}}}(\theta_n, 0) T_{\ell, |\mathbf{r}_0|\hat{\mathbf{z}}}^{s,L}(\theta_n, 0) \right|$$

368 which is equivalent to the 1D case considered in Section 3.1. Retrieving the Fourier  
 369 coefficients of the plane wave in the case  $\hat{\mathbf{r}} = \hat{\mathbf{z}}$  from (3.11) and numerically com-  
 370 puting exactly the low frequencies of the modified transfer function as described in  
 371 Section 3.2, then (3.9) leads to

$$|\varepsilon_I^\theta| = 4\pi^2 \left| \sum_{|n| \geq N_\theta/2} \tilde{T}_n^{s,n} J_{\mp n}(\kappa|\mathbf{r}|) - \sum_{|n| < N_\theta/2} \sum_{m \neq 0} \tilde{T}_n^{s,n+mN_\theta} J_{\mp(n+mN_\theta)}(\kappa|\mathbf{r}|) \right|$$

372 where  $\tilde{T}_n^s = \mathcal{F}_n^\theta[T_{\ell, |\mathbf{r}_0|\hat{\mathbf{z}}}^s(\theta, 0)]$ . Due to the very fast decay of the Bessel functions, we  
 373 find it is sufficient to apply the triangle inequality and keep only the lowest order  
 374 Bessel function terms:

$$|\varepsilon_I^\theta| \leq 4\pi^2 \sum_{n=-\infty}^{\infty} |\tilde{T}_n^s| |J_{M(N_\theta, n)}(\kappa|\mathbf{r}|)| \quad (3.13)$$

375 where

$$M(N_\theta, n) = \begin{cases} N_\theta - |n| & |n| < N_\theta/2 \\ |n| & |n| \geq N_\theta/2 \end{cases} \quad (3.14)$$

376 Equation (3.13) can be used to search for a value  $N_\theta$  via Algorithm 2.

377 Since  $N_\theta^{max}$  in Algorithm 2 is typically only a small constant larger than  $2\ell+1$ , the  
 378 algorithm as presented is dominated by the computation of the  $\mathcal{O}(\ell)$  modified transfer  
 379 function values and requires  $\mathcal{O}(\ell^2)$  operations. Important optimizations include using  
 380 more advanced searching methods (such as bisection), applying the symmetries  $\tilde{E}_m^* =$   
 381  $\tilde{E}_{-m}^*$  and  $\tilde{T}_m = \tilde{T}_{-m}$ , and taking advantage of the very fast decay of  $J_n$  to neglect  
 382 very small terms in the dot product.

```

1 Choose  $N_\theta^{max}$  sufficiently larger than  $2\ell + 1$ ;
2  $T_n \leftarrow T_{\ell, |\mathbf{r}_0| \hat{\mathbf{z}}}^{s,L}(\frac{2\pi n}{N_\theta^{max}}, 0)$ ,  $n = 0, \dots, N_\theta^{max} - 1$ ;
3  $\tilde{T}_n \leftarrow |\mathcal{F}_n^\theta[T]|$ ;
4  $\tilde{E}_n \leftarrow |J_n(\kappa |\mathbf{r}|)|$ ;
5 for  $N_\theta$  from  $2\ell$  to  $N_\theta^{max}$  by 2 do
6    $\tilde{E}_n^* \leftarrow \tilde{E}_{M(N_\theta, n)}$ ;
7   if  $\tilde{E}_n^* \cdot \tilde{T} < \varepsilon/4\pi^2$  then
8      $\lfloor$  return  $N_\theta$ 

```

**Algorithm 2:** Pseudocode to compute  $N_\theta$  given  $\ell$ ,  $|\mathbf{r}_0|$ , and  $|\mathbf{r}|$ .

383 **3.3.2. Choosing  $N_\phi$ .** After determining an appropriate  $N_\theta$ , letting  $N_\phi$  be a  
384 function of  $\theta$  allows reducing the number of quadrature points without affecting the  
385 error. The worst-case for the integration error in terms of  $N_\phi$  occurs when  $\mathbf{r}$  and  $\mathbf{r}_0$   
386 are in the  $xy$ -plane. Without loss of generality, suppose  $\hat{\mathbf{r}} = \hat{\mathbf{x}}$ . Then, for a fixed  $\theta_n$ ,  
387 the plane-wave (3.11) can be expressed as

$$E_{\mathbf{r}}(\theta_n, \phi) = e^{i\kappa \hat{\mathbf{s}}(\theta_n, \phi) \cdot \mathbf{r}} = \sum_{m=-\infty}^{\infty} i^m J_m(\kappa |\mathbf{r}| \sin(\theta_n)) e^{im\phi} \quad (3.15)$$

388 Since  $J_m(\kappa |\mathbf{r}| \sin(\theta_n))$  is exponentially small when  $m \gtrsim \kappa |\mathbf{r}| \sin(\theta_n)$ , the series can be  
389 truncated at  $N_\phi(\theta_n) \sim \kappa |\mathbf{r}| \sin(\theta_n)$  without incurring any appreciable error provided  
390 that the exact Fourier coefficients of  $T_{\ell, \mathbf{r}_0}^{s,L}(\theta, \phi)$  in  $\phi$  are available. This is the case  
391 since  $T_{\ell, \mathbf{r}_0}^{s,L}$  is bandlimited in  $\phi$ . Additionally, letting  $N_\phi$  be a function of  $\theta$  requires a  
392 final step in the computation of the modified transfer function. Section 3.2 computed  
393 the transfer function on a  $N_\theta/2+1 \times N_\phi$  grid. With  $N_\phi \rightarrow N_\phi(\theta_n)$ , the data computed  
394 for each  $\theta_n$  must be Fourier antepolated from length  $N_\phi$  to length  $N_\phi(\theta_n)$ .

395 Estimates of  $N_\phi(\theta_n)$  can be developed by determining when  $J_m(\kappa |\mathbf{r}| \sin(\theta_n))$   
396 becomes exponentially small, as in the computation of the EBF in [3]. However, we  
397 find that the EBF generated quadrature typically overestimates the sampling rate.  
398 To accurately compute  $N_\phi(\theta_n)$  a similar procedure to that in Section 3.3.1 is applied.  
399 After determining the appropriate  $N_\theta$ , the  $T_{\ell, \mathbf{r}_0}^{s,L}$  can be computed. For a given  $\theta$ , the  
400 error is

$$\left| \varepsilon_I^\phi \right| = \left| \int_0^{2\pi} E_{\pm|\mathbf{r}|\hat{\mathbf{x}}}(\theta, \phi) T_{\ell, \pm|\mathbf{r}_0|\hat{\mathbf{x}}}^{s,L}(\theta, \phi) d\phi - \frac{2\pi}{N_\phi(\theta)} \sum_{m=1}^{N_\phi(\theta)} E_{\pm|\mathbf{r}|\hat{\mathbf{x}}}(\theta, \phi_m) T_{\ell, \pm|\mathbf{r}_0|\hat{\mathbf{x}}}^{s,LL}(\theta, \phi_m) \right|$$

401 where  $T^{s,LL}$  is the bandlimited modified transfer function with both the  $\theta$ -frequencies  
402 and  $\phi$ -frequencies truncated for the quadrature. That is, if

$$T_{\ell, \mathbf{r}_0}^s(\theta, \phi) = \frac{1}{2} T_{\ell, \mathbf{r}_0}(\theta, \phi) |\sin(\theta)| = \sum_{n=-\infty}^{\infty} \sum_{m=-\ell}^{\ell} \tilde{T}_{n,m}^s e^{n\theta+m\phi}$$

403 then

$$T_{\ell, \mathbf{r}_0}^{s,L}(\theta, \phi) = \sum_{n=-N_\theta/2+1}^{N_\theta/2-1} \sum_{m=-\ell}^{\ell} \tilde{T}_{n,m}^s e^{n\theta+m\phi}$$

404 and

$$T_{\ell, \mathbf{r}_0}^{s, LL}(\theta, \phi) = \sum_{n=-N_\theta/2+1}^{N_\theta/2-1} \sum_{m=-N_\phi(\theta_n)/2+1}^{N_\phi(\theta_n)/2-1} \tilde{T}_{n,m}^s e^{n\theta+m\phi}$$

405 We again apply the result of Section 3.1 by retrieving the Fourier coefficients of the  
 406 plane wave in the case  $\hat{\mathbf{r}} = \hat{\mathbf{x}}$  from Equation (3.15) and computing exactly the low  
 407 frequencies of the modified transfer function. Equation (3.9) leads to

$$|\varepsilon_I^\phi| \leq 2\pi \sum_{m=-\ell}^{\ell} \left| \tilde{T}_m^{s, L}(\theta) \right| |J_{M(N_\phi(\theta), m)}(\kappa |\mathbf{r}| \sin(\theta))| \quad (3.16)$$

408 Equation (3.16) can then be used to search for a value of  $N_\phi(\theta_n)$  via Algorithm 3.

```

1 Choose  $N_\phi^{max}$  sufficiently larger than  $2\ell + 1$ ;
2 for  $\theta_n, n = 0, \dots, N_\theta/2$ , do
3    $T_m \leftarrow T_{\ell, |\mathbf{r}_0| \hat{\mathbf{x}}}^{s, L}(\theta_n, \frac{2\pi m}{2\ell+1}), m = 0, \dots, 2\ell$ ;
4    $\tilde{T}_m \leftarrow |\mathcal{F}_m^\phi[T]|$ ;
5    $\tilde{E}_m \leftarrow |J_m(\kappa |\mathbf{r}| \sin(\theta_n))|$ ;
6   for  $N_\phi(\theta_n)$  from 4 to  $N_\phi^{max}$  by 4 do
7      $\tilde{E}_m^* \leftarrow \tilde{E}_{M(N_\phi(\theta_n), m)}$ ;
8     if  $\tilde{E}_m^* \cdot \tilde{T}_m < \varepsilon/4\pi^2$  then
9        $\lfloor$  Save  $N_\phi(\theta_n)$ 

```

**Algorithm 3:** Pseudocode to compute each  $N_\phi(\theta_n)$  given  $\ell$ ,  $|\mathbf{r}_0|$ ,  $|\mathbf{r}|$ , and  $N_\theta$ .

409 Since  $N_\phi^{max}$  is only a small constant larger than  $2\ell + 1$ , the algorithm as presented  
 410 is dominated by the computation of the modified transfer function and requires  $\mathcal{O}(\ell^3)$   
 411 operations. Optimizations similar to those presented in Section 3.3.1 can be applied.  
 412 Using the EBF as an initial guess in the search for  $N_\phi(\theta_n)$  further improves the  
 413 searching speed. Additionally, only half of the  $N_\phi(\theta_n)$ 's may be computed due to  
 414 symmetry about the  $z = 0$  plane.

415 **3.3.3. Choosing  $|\mathbf{r}|$  and  $|\mathbf{r}_0|$ .** The previous algorithms require representative  
 416 values of  $|\mathbf{r}|$  and  $|\mathbf{r}_0|$  for each level of the tree. The worst-case transfer vectors,  $\mathbf{r}_0$ ,  
 417 are those with smallest length. If  $a_l$  is the box size at level  $l$ , then  $|\mathbf{r}_0| = 2a_l$  is the  
 418 smallest transfer vector length in the common one buffer-box case.

419 The worst-case value of  $|\mathbf{r}|$  is the largest. For a box of size  $a_l$ ,  $|\mathbf{r}| \leq a_l\sqrt{3}$ .  
 420 However, using  $|\mathbf{r}| = a_l\sqrt{3}$  in the previous methods is often too conservative. This  
 421 case only occurs when two points are located in the exact corners of the boxes – a  
 422 very rare case. See Figure 3.5. Instead, we let  $|\mathbf{r}| = \alpha a_l\sqrt{3}$  for some  $\alpha \in [0, 1]$ . A  
 423 high  $\alpha$  guarantees an upper bound on the error generated by the quadrature, but the  
 424 points which actually generate this error become increasingly rare. A lower value of  
 425  $\alpha$  will yield a smaller quadrature, but more points may fall outside the radius  $|\mathbf{r}|$  for  
 426 which the upper bound on the error is guaranteed.

427 **3.3.4. Number of Quadrature Points.** Recall from Section 2.2 that the typical  
 428 approach in the FMM is to use  $N + 1$  uniform points in the  $\phi$  direction and  $\frac{N+1}{2}$



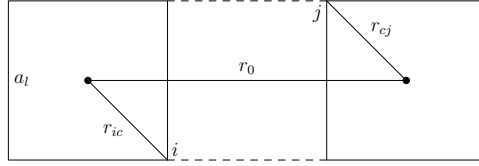


FIG. 3.5. The worst-case  $\mathbf{r}$  and  $\mathbf{r}_0$ , projected from the 3D box. Here,  $|\mathbf{r}_0| = 2a_l$  and  $i$  and  $j$  are on the opposite corners of the box so that  $|\mathbf{r}| = |\mathbf{r}_{ic}| + |\mathbf{r}_{cj}| = a_l\sqrt{3}$ .

429 Gauss-Legendre points in the  $\theta$  direction so that all  $Y_n^m$ ,  $-n \leq m \leq n$ ,  $0 \leq n \leq N$   
 430 are integrated exactly. In [16], Chew et al. takes  $\frac{N+1}{2} = \ell + 1$ , which is an approx-  
 431 imate choice based on the rapid decay of the coefficients in the spherical harmonics  
 432 expansion of a plane-wave. This results in approximately

$$K_{sh} = 2(\ell + 1)^2 \sim 2\ell^2$$

433 quadrature points.

434 For a given Gegenbauer series truncation  $\ell$ , the total number of quadrature points  
 435 required in the Fourier based FMM is approximately

$$\begin{aligned} K_{fb} &\approx \frac{N_\theta}{2} \frac{1}{\pi} \int_0^\pi N_\phi(\theta) d\theta \\ &\approx (\ell + C_1) \frac{1}{\pi} \int_0^\pi (2\ell + C_2(\theta)) \sin(\theta) d\theta \end{aligned}$$

436 where  $C_1, C_2 \geq 1$  are small integers dependent on  $\ell$ , numerically computed from the  
 437 methods in Section 3.3.1, 3.3.2. Keeping only the leading term in  $\ell$ :

$$K_{fb} \sim \frac{4}{\pi} \ell^2 \approx 1.3 \ell^2$$

438 Thus, the method presented in this paper uses approximately 0.64 times the number  
 439 of quadrature points in the standard FMM. However, it is possible that the same  $N_\phi$   
 440 optimization can be applied to the standard FMM for the same reasons it was applied  
 441 in Section 3.3.2 to reduce the standard quadrature to a comparable size.

442 **3.4. Interpolation and Anterpolation.** Most importantly, the Fourier based  
 443 FMM directly uses FFTs in the interpolation and anterpolation steps. This makes the  
 444 time critical upward pass and downward pass efficient and easy to implement while  
 445 retaining the exactness of global methods.

446 Characterize a quadrature by an array of length  $N_\theta/2 + 1$ ,

$$K = [N_\phi(\theta_0), N_\phi(\theta_1), \dots, N_\phi(\theta_{N_\theta/2-1}), N_\phi(\theta_{N_\theta/2})]$$

447 noting that  $N_\phi(\theta_n) = N_\phi(\theta_{N_\theta/2+n})$ . The data  $F(\theta_n, \phi_m)$  sampled on a quadrature  
 448  $K$  is transformed to another quadrature  $K'$  by performing a sequence of Fourier  
 449 interpolations and anterpolations. Let

$$\mathcal{N}_\phi = \max \left[ \max_{0 \leq n \leq N_\theta/2} N_\phi(\theta_n), \max_{0 \leq n \leq N'_\theta/2} N'_\phi(\theta_n) \right]$$

450 Then, the following steps, as illustrated in Figure 3.6, perform an exact interpola-  
 451 tion/anterpolation using only FFTs.

- 452 1. For each  $\theta_n$ ,  $0 \leq n \leq N_\theta/2$ , Fourier interpolate the data  $[F(\theta_n, \phi_m)]_{m=0}^{N_\phi(\theta_n)-1}$   
 453 from length  $N_\phi(\theta_n)$  to  $\mathcal{N}_\phi$ .  
 454 2. For each  $\phi_m$ ,  $0 \leq m < \mathcal{N}_\phi/2$ , apply symmetry (3.6) to construct the  $\theta$ -  
 455 periodic sequences  $[F(\theta_n, \phi_m)]_{n=0}^{N_\theta-1}$ .  
 456 3. For each  $\phi_m$ ,  $0 \leq m < \mathcal{N}_\phi/2$ , Fourier interpolate the data  $[F(\theta_n, \phi_m)]_{n=0}^{N_\theta-1}$   
 457 from length  $N_\theta$  to  $N'_\theta$ .  
 458 4. For each  $\theta_n$ ,  $0 \leq n \leq N'_\theta/2$ , apply symmetry (3.6) to construct the  $\phi$ -periodic  
 459 sequences  $[F(\theta_n, \phi_m)]_{m=0}^{\mathcal{N}_\phi-1}$ .  
 460 5. For each  $\theta_n$ ,  $0 \leq n \leq N'_\theta/2$ , Fourier antepolate the data  $[F(\theta_n, \phi_m)]_{m=0}^{\mathcal{N}_\phi-1}$   
 461 from length  $\mathcal{N}_\phi$  to  $N'_\phi(\theta_n)$ .

462 A slightly more efficient algorithm uses the symmetry (3.5) rather than (3.6).

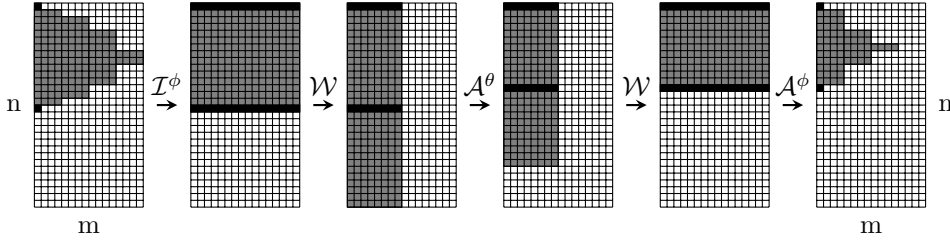


FIG. 3.6. The data profile at each step in an antepolation from a large quadrature  $K$  with  $N_\theta = 30$  to a smaller quadrature  $K'$  with  $N'_\theta = 24$ . The data corresponding to a pole has been darkened for clarity.

463 **3.5. Numerical Results.** In the following sections, we will use the total mea-  
 464 sured error,  $\varepsilon_T$ , defined as

$$\varepsilon_T = \frac{e^{i\kappa|\mathbf{r}+\mathbf{r}_0|}}{|\mathbf{r}+\mathbf{r}_0|} - \sum_{n=1}^{N_\theta} \frac{4\pi^2}{N_\theta N_\phi(\theta_n)} \sum_{m=1}^{N_\phi(\theta_n)} E_{\mathbf{r}}(\theta_n, \phi_m) T_{\ell, \mathbf{r}_0}^{\mathbf{s}, L}(\theta_n, \phi_m) \quad (3.17)$$

465 The total Gegenbauer truncation error,  $\varepsilon_G$ , is

$$\varepsilon_G = \frac{e^{i\kappa|\mathbf{r}+\mathbf{r}_0|}}{|\mathbf{r}+\mathbf{r}_0|} - i\kappa \sum_{n=0}^{\ell} (-1)^n (2n+1) h_n^{(1)}(\kappa|\mathbf{r}_0|) j_n(\kappa|\mathbf{r}|) P_n(\hat{\mathbf{r}} \cdot \hat{\mathbf{r}}_0) \quad (3.18)$$

466 The total integration error  $\varepsilon_I$  is

$$\varepsilon_I = \varepsilon_T - \varepsilon_G \quad (3.19)$$

467 **3.5.1. Single-Level Error.** In the first test case, shown in Figure 3.7, we exam-  
 468 ine the choice of  $N_\theta$  by using the worst case  $\mathbf{r}_0 = |\mathbf{r}_0| \hat{\mathbf{z}}$ . Here, the optimal Gegenbauer  
 469 truncation  $\ell$  is obtained as explained in Section 2.1 [see Equation (2.6)]. The quadra-  
 470 ture for computing the integral (3.1) was constructed as described in Section 3.3.  
 471 With box size  $a = 1$ , the quadrature and Gegenbauer truncation are constructed with  
 472  $|\mathbf{r}| = 0.8a\sqrt{3}$ ,  $|\mathbf{r}_0| = 2a$ , and target error  $\varepsilon = 10^{-4}$ ,  $10^{-8}$ . The plotted errors represent  
 473 the maximum found over many directions  $\hat{\mathbf{r}}$ , verifying that the worst case is  $\mathbf{r} \sim \pm \hat{\mathbf{z}}$ .

474 We note that the target error  $\varepsilon$  is accurately achieved, for all frequencies (except  
 475 in the low-frequency breakdown because of round off errors). The actual error is  
 476 within a factor of 2 or less of the target error. The increase in error for small box

477 sizes corresponds to the low frequency breakdown when the transfer function has very  
 478 large amplitude and roundoff errors become dominant. In this regime the quadrature  
 479 target error bound can also be relaxed to improve efficiency — it is inefficient to have  
 480 a large quadrature that provides a small integration error when the transfer function  
 481 cannot provide comparable accuracy.

482 We also show a comparison with a simple heuristic for choosing  $N_\theta$ . Based on  
 483 the truncation of the Gegenbauer series, we expect  $N_\theta = 2\ell + 1$  (rounded up to the  
 484 nearest multiple of 2) to be a reasonable guess. The error resulting from this choice  
 485 is shown by the curve labeled  $\varepsilon_I^{ebf}$ . This shows that our scheme produces a more  
 486 accurate estimate of this parameter and, in particular, with our scheme, we no longer  
 487 see the drift in error seen with  $\varepsilon_I^{ebf}$ .

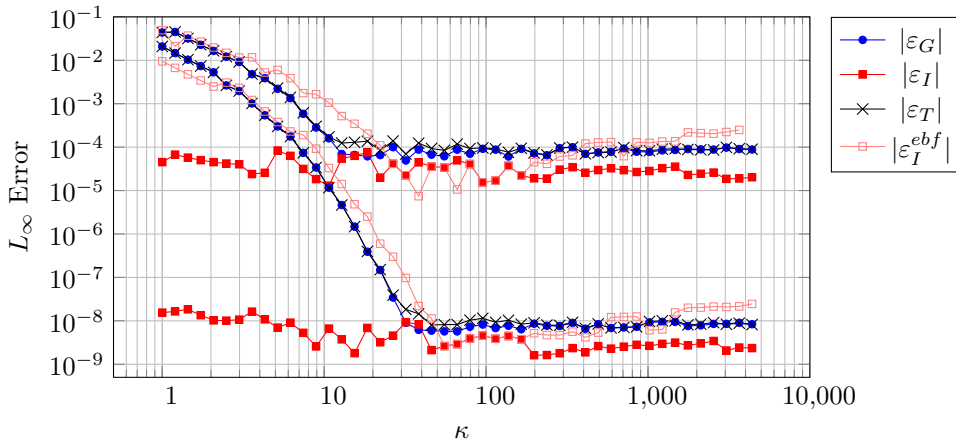


FIG. 3.7. Results with  $\mathbf{r}_0 \sim \hat{\mathbf{z}}$ , target accuracy  $\varepsilon = 10^{-4}$  and  $\varepsilon = 10^{-8}$ , the Gegenbauer truncation chosen as in Section 2.1,  $N_\theta$  chosen as in Section 3.3.1, and box size  $a = 1$ . The  $\varepsilon_I^{ebf}$  curve corresponds to using the EBF along with  $N_\theta = 2\ell + 1$ ; this choice leads to a drift in the error as the frequency increases. In contrast, using our error estimate and scheme to choose the parameters, the error follows closely the target error.

488 The second test case, shown in Figure 3.8, shows the accuracy resulting from  
 489 our choice of  $N_\phi$  using the worst case  $\mathbf{r}_0 = |\mathbf{r}_0| \hat{\mathbf{x}}$ . Again, the direct computation was  
 490 used to find the optimal Gegenbauer truncation  $\ell$  and the quadrature was constructed  
 491 following Section 3.3. With box size  $a = 1$ , the quadrature and Gegenbauer truncation  
 492 are constructed with  $|\mathbf{r}| = 0.8a\sqrt{3}$ ,  $|\mathbf{r}_0| = 2a$ , and target error  $\varepsilon = 10^{-4}$  and  $10^{-8}$ .  
 493 The plotted errors represent the maximum found over many directions  $\hat{\mathbf{r}}$ , verifying  
 494 that the worst case is  $\mathbf{r} \sim \pm \hat{\mathbf{x}}$ . We can see that the target error is achieved even more  
 495 accurately than the  $\hat{\mathbf{z}}$  case. This is due to the number of  $N_\phi$  that are chosen — one  
 496 for each  $\theta_n$ . The  $N_\phi(\theta_n)$  that yields the most inaccurate result dominates the others,  
 497 bringing the integration error very close to the target. The comparison heuristic is  
 498  $\varepsilon_I^{ebf}$  uses the constant  $N_\phi = 2\ell + 1$  (rounded up to the nearest multiple of 4). Again,  
 499 the target error should be relaxed in the low frequency breakdown regime.

500 Figure 3.9 shows the ratio of the number of points in the quadrature used in  
 501 Figure 3.8 to the number of quadrature points that would be used in a typical spherical  
 502 harmonics based FMM using the same Gegenbauer truncation  $\ell$  chosen by the direct  
 503 calculation. The procedures presented in this paper result in a quadrature which is  
 504 substantially smaller than what would typically be used. Notably, the analysis in

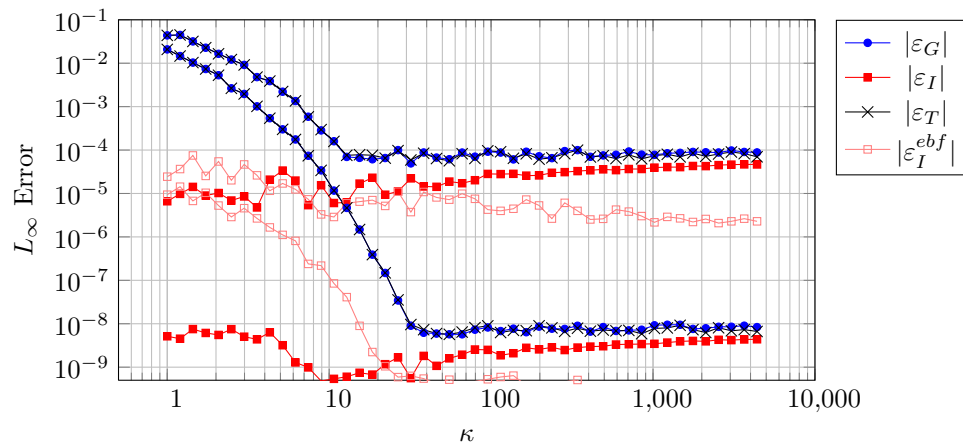


FIG. 3.8. Results with  $\mathbf{r}_0 \sim \hat{\mathbf{x}}$ , target accuracy  $\varepsilon = 10^{-4}$  and  $\varepsilon = 10^{-8}$ , the Gegenbauer truncation chosen as in Section 2.1,  $N_\theta$  and  $N_\phi$  chosen as in Section 3.3.1 and 3.3.2, and box size  $a = 1$ . The  $\varepsilon_I^{ebf}$  curve corresponds to using the EBF along with  $N_\phi(\theta_n) = 2\ell + 1$ ; this choice greatly overestimates the size of the quadrature needed in the  $\phi$ -direction especially near the poles  $\theta = \{0, \pi\}$ . In contrast, using our error estimate and scheme to choose the parameters, the error follows closely the target error.

505 Section 3.3.4 is supported.

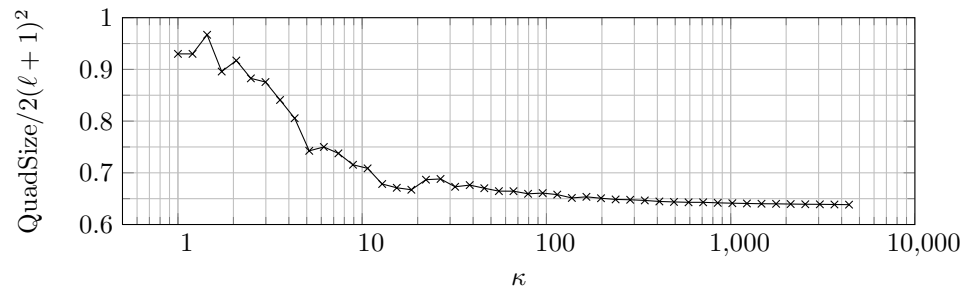


FIG. 3.9. The ratio of the number of quadrature points required in the Fourier based FMM and what would be used in a typical spherical harmonics based FMM for the same  $\ell$ . The curve asymptotes close to  $2/\pi \approx 0.64$  as expected from Section 3.3.4

506 Together, these results demonstrate that by choosing  $\ell$  and the quadrature as  
 507 presented in this paper, the error is controlled and the quadrature size is chosen  
 508 nearly optimally. The accurate error bounds derived in Section 3.3 means that we  
 509 can provide a sharp bound of the total final error of the method and optimize the  
 510 running time of the method for that prescribed error. A reduction in the quadrature  
 511 size improves memory usage and suggests an improved running time over similar  
 512 algorithms.

513 **3.5.2. Multi-Level Error.** The previous section verified the error bounds de-  
 514 rived for a single level. In this section, we show that the method performs as expected  
 515 in the multilevel case as well. We considered two points distributed as in Figure 3.5,  
 516 at opposite corners of the box. The transfer pass (M2L) is always done at the highest  
 517 level in the tree (level 2). Then, the number of levels is increased, thereby adding

518 additional translation steps to the calculation. This test therefore checks that the  
 519 Fourier based interpolation and anterpolation procedure (Section 3.4) does not affect  
 520 the accuracy of the calculation.

521 Figure 3.10 shows the convergence of the method as the target error is adjusted,  
 522 thereby changing  $\ell$  and the quadrature size appropriately. We show  $\varepsilon_G^L$  (Gegenbauer  
 523 truncation),  $\varepsilon_T^L$  (total error), and  $\varepsilon_I^L$  (interpolation error obtained as the difference  
 524 between  $\varepsilon_G^L$  and  $\varepsilon_T^L$ ), for  $L = 2, \dots, 8$  ( $L$  is the total number of levels). The quadrature  
 525 size is the total number of quadrature points at the highest active level, with box size  
 526  $a_2 = 1$ . Note that for  $L = 2$  there is only one active level and no translation step.  
 527 On the same plot, we show the discrepancy between  $\varepsilon_I^L$  ( $L = 3, \dots, 8$ ) and  $\varepsilon_I^2$  which  
 528 corresponds to the error due to the upward and downward passes. We expect this  
 529 error to be much smaller than the target error, since the target error accounts for the  
 530 M2L operation and therefore the quadrature is over-estimated when considering only  
 531 the translation functions. This is confirmed by Figure 3.10. The curve  $\varepsilon_G^L$  is exactly  
 532 the same for all  $L$  while  $\varepsilon_T^L$  has small variations with  $L$  due to the sampling of the  
 533 translation function in the updownward and downward passes.

534 We note that the method converges super-exponentially, following the rate of  
 535 decay of the Jacobi-Anger series (3.11).

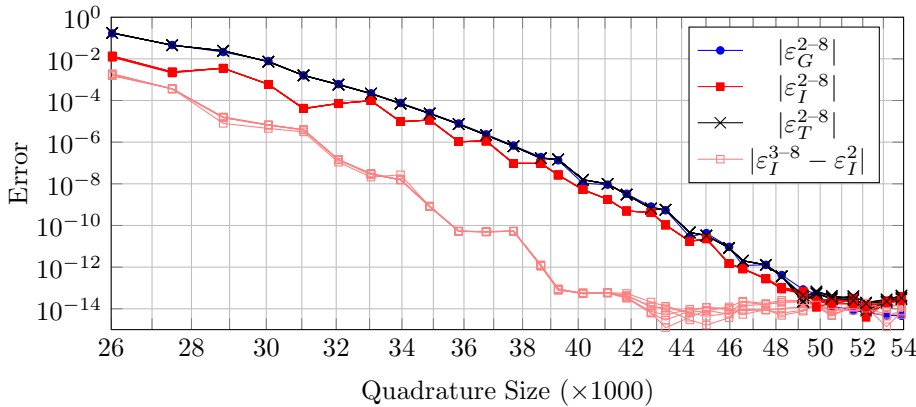


FIG. 3.10. Log-log plot of two-level convergence with  $\kappa = 100$ ,  $\alpha = 0.8$ , and highest active level box size  $a_2 = 1$ . For each curve, we have 7 cases with  $L = 2, \dots, 8$ . This is denoted by 2–8 in the legend of the figure. The 7 cases are nearly undistinguishable except when the error is of order  $10^{-12}$  and below.

536 To further show that the numerical integral is converging to the Gegenbauer series value,  
 537 Figure 3.11 sets the Gegenbauer error to a constant and uses the target error to increase the quadrature size only. We observe that as the quadrature size  
 538 increases the total error becomes exactly equal to the Gegenbauer series truncation  
 539 error. For this case, we used two active levels for the MLFMM, therefore including  
 540 the FFT interpolation and anterpolation stages. This validates numerically our theoretical  
 541 analysis and shows that the error caused by our anterpolation strategy and  
 542 smoothing of the transfer function  $T_{\ell, r_0}^s(\theta, \phi)$  can be effectively controlled and behaves  
 543 as expected.  
 544

545 **3.5.3. Speed.** As discussed in Section 3.4, the Fourier based FMM uses only  
 546 FFTs in the upward pass and downward pass to perform the interpolations and anterpolations.  
 547 FFTs make these steps easier to implement and very efficient. In addi-

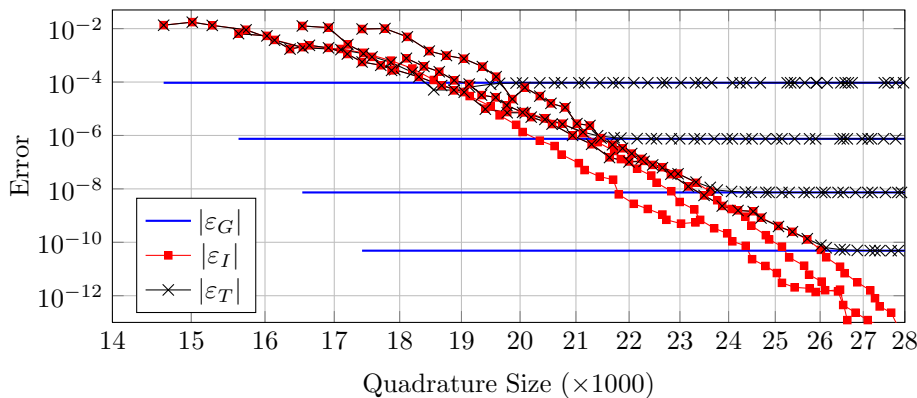


FIG. 3.11. Log-log plot of two-level convergence to the truncated Gegenbauer series value with  $\kappa = 100$ ,  $\alpha = 1/\sqrt{3}$ , and highest active level box size  $a_2 = 1$ . The convergence of the numerical quadrature for  $(\theta, \phi)$  (red curves) should be compared with the convergence of the toy problem in Figure 3.2 (blue curve in Figure 3.2).

tion, Section 3.3.4 and Figure 3.9 suggest that the quadrature used in this paper is significantly smaller than what is typically used for a spherical harmonic basis.

All times reported are from repeated runs on a 2.93GHz Intel Core i7 Quad Core Processor 870 with 8MB Cache with 8GB of 1333MHz DDR3 RAM.

First, we illustrate the efficient use of FFTs in the interpolation and anterpolation stages. Here, we compare the FFT interpolation method of Section 3.4 against the semi-naïve exact spherical harmonic interpolation method which consists of a forward FFT in  $\phi$ , a dense matrix-matrix product on the  $\theta$  angles, and a backward FFT in  $\phi$ . This spherical harmonics method is analyzed and accelerated in [14, 7]. Figure 3.12 confirms the expected asymptotic running times of each method.

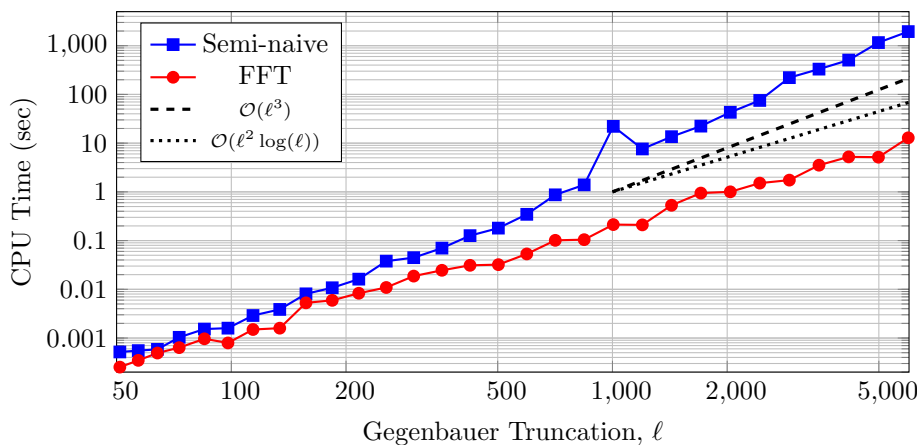


FIG. 3.12. Comparison of the FFT interpolation scheme of Section 3.4 [complexity  $\mathcal{O}(\ell^2 \log \ell)$ ] with the semi-naïve  $\mathcal{O}(\ell^3)$  spherical harmonic transform described in [14].

To show that the optimal asymptotic running time is achieved, Figure 3.13 shows the recorded running times of the Fourier based FMM and the direct matrix-vector product. The target error is set to  $10^{-4}$  with  $\alpha = 1$  and is achieved in every case. For

561  $N = 8.2 \cdot 10^6$  the points are uniformly distributed in a cube with side length  $80\lambda$ . The  
 562 wave number  $\kappa$  is scaled with  $N^{1/3}$  to provides a nearly constant density of points  
 563 per wavelength as  $N$  is varied. As expected, by choosing the correct number of levels  
 564 the running time is asymptotically  $\mathcal{O}(N)$  as  $N$  is increased with a constant number  
 565 of points per wavelength. Note that the cross-over point is  $N \approx 3,000$ .

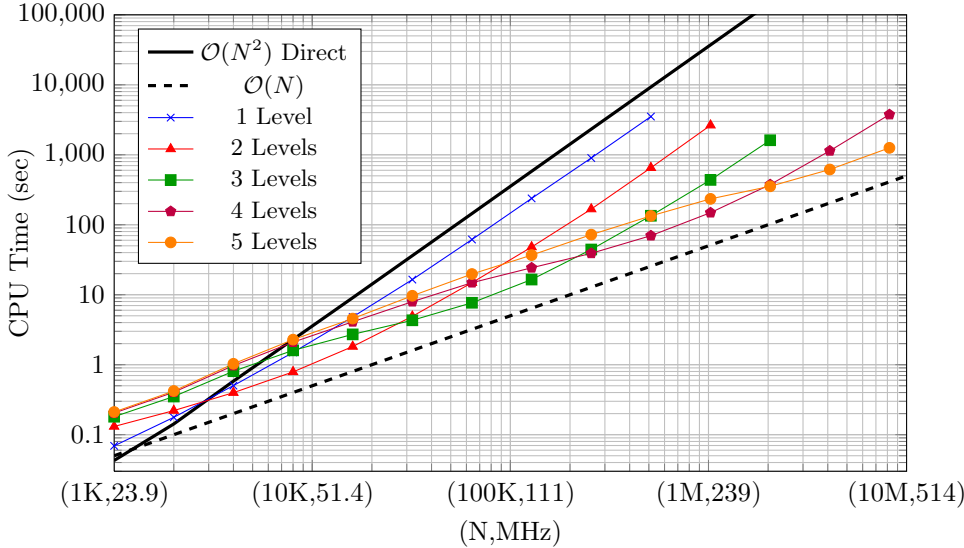


FIG. 3.13. Average running times of the Fourier based FMM for constant number of volumetric points per wavelength. By choosing the optimal number of levels, we achieve an  $\mathcal{O}(N)$  complexity.

566 **4. Conclusion.** We have proposed using the Fourier basis  $e^{ip\phi}e^{iq\theta}$  in the spheri-  
 567 cal variables  $\phi$  and  $\theta$  to represent the far-field approximation in the FMM. By ap-  
 568 proximating the Helmholtz kernel with Equation (1.1) and using a uniform quadra-  
 569 ture we can take advantage of very fast, exact, and well-known FFT interpola-  
 570 tion/antepolation methods. By exploiting symmetries and a scheme to reduce the  
 571 number of points in the  $\phi$ -direction, the total number of uniform quadrature points re-  
 572 quired is smaller than the number of Gauss-Legendre quadrature points typically used  
 573 with spherical harmonics. This is realized by removing the high frequency compo-  
 574 nents of the modified transfer function,  $T_{\ell, \mathbf{r}_0}^s(\theta, \phi)$ , during the precomputation phase  
 575 which do not significantly contribute to the final integration.

576 The Fourier based FMM approach has a number of advantages. Since the inter-  
 577 polation and antepolation algorithms are exact, the error analysis is simplified; we  
 578 establish a sharp upper bound for the error. The key parameters are the Gegenbauer  
 579 truncation parameter  $\ell$  and the quadrature size, in particular the sampling rate in the  
 580  $\theta$ -direction. The truncation error  $\varepsilon_G$  has been extensively studied by other authors  
 581 and is well understood. The integration error  $\varepsilon_I$  accounts for the bandlimited approx-  
 582 imation of the modified transfer function and the finite sampling of the plane-waves.  
 583 This error can be accounted for a priori during the precomputation stage. Numerical  
 584 tests have confirmed that this error analysis is quite sharp. Constructive algorithms to  
 585 find nearly optimal parameters were proposed. Since highly efficient FFT algorithms  
 586 are available in virtually every computing environment, the time-critical interpolation  
 587 stages of the algorithm are much easier to implement efficiently.

588 **Acknowledgments.** This research was supported by the U.S. Army Research  
 589 Laboratory, through the Army High Performance Computing Research Center, Co-  
 590 operative Agreement W911NF-07-0027, the Stanford School of Engineering, and the  
 591 King Abdullah University of Science and Technology.

## REFERENCES

- 592
- 593 [1] Q. CARAYOL AND F. COLLINO, *Error estimates in the fast multipole method for scattering prob-*  
 594 *lems. Part 1: Truncation of the Jacobi-Anger series*, ESAIM: M2NA, 38 (2004), pp. 371–  
 595 394.
- 596 [2] ———, *Error estimates in the fast multipole method for scattering problems. Part 2: Truncation*  
 597 *of the Gegenbauer series*, ESAIM: M2NA, 39 (2004), pp. 183–221.
- 598 [3] W.C. CHEW, E. MICHIELSSEN, J. M. SONG, AND J. M. JIN, eds., *Fast and Efficient Algorithms*  
 599 *in Computational Electromagnetics*, Artech House, Inc., Norwood, MA, USA, 2001.
- 600 [4] INDRANIL CHOWDHURY AND VIKRAM JANDHYALA, *Integration and interpolation based on fast*  
 601 *spherical transforms for the multilevel fast multipole method*, Microwave and Optical Tech-  
 602 *nology Letters*, 48 (2006), pp. 1961–1964.
- 603 [5] R. COIFMAN, V. ROKHLIN, AND S. WANDZURA, *The fast multipole method for the wave equation:*  
 604 *A pedestrian prescription*, Antennas and Propag. Magazine, IEEE, 35 (1993), pp. 7–12.
- 605 [6] ERIC DARVE, *The fast multipole method I: Error analysis and asymptotic complexity*, SIAM J.  
 606 *Numer. Anal.*, 38 (2000), pp. 98–128.
- 607 [7] ———, *The fast multipole method: Numerical implementation*, J. Comput. Phys., 160 (2000),  
 608 pp. 195–240.
- 609 [8] JAMES R. DRISCOLL AND D.M. HEALY, *Computing Fourier transforms and convolutions on the*  
 610 *2-sphere*, Adv. Appl. Math., 15 (1994), pp. 202–250.
- 611 [9] A. DUTT, M. GU, AND V. ROKHLIN, *Fast algorithms for polynomial interpolation, integration,*  
 612 *and differentiation*, SIAM J. Numer. Anal., 33 (1996), pp. 1689–1711.
- 613 [10] N. ENGHETA, W. D. MURPHY, V. ROKHLIN, AND M. S. VASSILIOU, *The fast multipole method*  
 614 *(FMM) for electromagnetic scattering problems*, IEEE Trans. Antennas Propag., 40 (1992),  
 615 p. 634.
- 616 [11] O. ERGUL AND L. GUREL, *Optimal interpolation of translation operator in multilevel fast mul-*  
 617 *tiple algorithm*, IEEE Trans. Antennas Propag., 54 (2006), pp. 3822–3826.
- 618 [12] M. L. HASTRITER, S. OHNUKI, AND W. C. CHEW, *Error control of the translation operator in*  
 619 *3D MLFMA*, Microwave and Optical Technology Letters, 37 (2003), pp. 184–188.
- 620 [13] D.M. HEALY, D. ROCKMORE, P.J. KOSTELEK, AND S. MOORE, *FFTs for the 2-sphere - im-*  
 621 *provements and variations*, J. Fourier Analysis and Applications, 9 (2003), pp. 341–385.
- 622 [14] RÜDIGER JAKOB-CHIEN AND BRADLEY K. ALPERT, *A fast spherical filter with uniform resolu-*  
 623 *tion*, J. Comput. Phys., 136 (1997), pp. 580–584.
- 624 [15] J. KNAB, *Interpolation of bandlimited functions using the approximate prolate series (corresp.)*,  
 625 *Information Theory*, IEEE, 25 (1979), pp. 717–720.
- 626 [16] S. KOC, J. M. SONG, AND W. C. CHEW, *Error analysis for the numerical evaluation of the*  
 627 *diagonal forms of the scalar spherical addition theorem*, SIAM J. Numer. Anal., 36 (1999),  
 628 pp. 906–921.
- 629 [17] E. MCKAY HYDE AND OP BRUNO, *A fast higher-order solver for scattering by penetrable bodies*  
 630 *in three dimension*, J. Comp. Phys., 202 (2005), pp. 236–261.
- 631 [18] J. RAHOLA, *Diagonal forms of the translation operators in the fast multipole algorithm for*  
 632 *scattering problems*, BIT, 36 (1996), pp. 333–358.
- 633 [19] V. ROKHLIN, *Rapid solution of integral equations of scattering theory in two dimensions*, J.  
 634 *Comput. Phys.*, 86 (1990), pp. 414–439.
- 635 [20] ———, *Diagonal forms of translation operators for the Helmholtz equation in three dimensions*,  
 636 *Applied and Computational Harmonic Analysis*, 1 (1993), pp. 82–93.
- 637 [21] V. ROKHLIN AND M. TYGERT, *Fast algorithms for spherical harmonic expansions*, SIAM J.  
 638 *Scientific Computing*, 27 (2006), pp. 1903–1928.
- 639 [22] JUKKA SARVAS, *Performing interpolation and antepolation entirely by fast Fourier transform*  
 640 *in the 3-D multilevel fast multipole algorithm*, SIAM J. Numer. Anal., 41 (2003), pp. 2180–  
 641 2196.
- 642 [23] NICO SNEEUW AND RICHARD BUN, *Global spherical harmonic computation by two-dimensional*  
 643 *fourier methods*, Journal of Geodesy, 70 (1996), pp. 224–232. 10.1007/BF00873703.
- 644 [24] RELJI SUDA AND MASAYASU TAKAMI, *A fast spherical harmonics transform algorithm*, Math.  
 645 *of Comp.*, 71 (2001), pp. 703–715.